# 9. Subsurface Temperatures beneath Southern Hydrate Ridge[1]

Anne M. Tréhu[2]

## ABSTRACT

During Ocean Drilling Program Leg 204, 80 in situ measurements of subseafloor temperature were made; 68 of these showed good frictional pulses on insertion and extraction from the seafloor and were used to constrain the subsurface temperature. Considering uncertainties from various sources, uncertainties in the in situ temperatures are estimated to generally be less than ±0.3°C. The data are consistent with a purely conductive temperature regime at all sites, and there is no resolvable difference in heat flow between sites on the flanks of southern Hydrate Ridge and sites near the summit, where other data indicate that free gas is venting into the ocean, gas hydrate is forming rapidly, and free gas and gas hydrate coexist in the sediments. We interpret this apparent paradox to indicate that the aqueous fluid flow is decoupled from free gas flow and that advection of free gas does not have a significant effect on the temperature field. The temperature data, which include several measurements within a few meters of the predicted base of the methane hydrate stability field (calculated for the measured pore water salinity at each site) also indicate that the bottom-simulating reflection (BSR) corresponds to the base of gas hydrate stability within measurement uncertainties, although a systematic shallowing of the BSR by as much as 10 m is possible. The heat flow indicated by the Leg 204 measurements and the regional BSR depth is significantly lower than the heat flow predicted based on the age of the subducting plate and the thickness of the accretionary complex. Several measurements made near the summit at depths shallower than 60 meters below seafloor show anomalous behavior consistent with low in situ thermal conductivity, possibly because of the presence of free gas and/or massive gas hydrate in these sediments.

# INTRODUCTION

Gas hydrate forms in marine sediments at low temperature and high pressure wherever enough methane or other hydrate-forming gas is present. The regional occurrence of a bottom-simulating reflection (BSR), which is generally interpreted to mark the boundary between sediments containing gas hydrate and sediments containing free gas, indicates the widespread occurrence of gas hydrate within the shallow subsurface beneath southern Hydrate Ridge. Drilling during Ocean Drilling Program (ODP) Leg 204, during which gas hydrate was found at all sites where a BSR was present, supports this inference. Figure F1 shows slices, extracted from a three-dimensional (3-D) seismic site survey, that pass through the Leg 204 drill sites. Overlain on the seismic data are estimates of the gas hydrate content of the sediment derived from a variety of different gas hydrate proxies (Tréhu et al., 2004a). Gas hydrate is generally not present in the upper 30–40 meters below seafloor (mbsf) except near the seafloor at the summit, where at least 25% of the total volume appears to be gas hydrate. Elsewhere, the average gas hydrate content of the sediment appears to be 2%–8%, except for localized regions just above the BSR, where the gas hydrate content may be somewhat higher. On a scale of centimeters, concentrations are more variable, with nearly 100% gas hydrate in lenses as thick as several centimeters (Tréhu, Bohrmann, Rack, and Torres, et al., 2003).

Several distinctive seismic reflections are labeled on Figure F1. Horizon A is a strong reflection that underlies the BSR beneath the northwestern flank of southern Hydrate Ridge. It is a coarse-grained, volcanic ash–rich horizon, 2–4 m thick, that is thought to be a conduit through which free gas is transported to the summit. Beneath the summit, gas pressure within Horizon A may equal or even exceed lithostatic pressure, enabling gas hydrate to migrate into and through the gas hydrate stability zone (GHSZ) (Tréhu et al., 2004b, Torres et al., 2004; Milkov et al., 2004). The results discussed below, however, suggest that the flow rate for aqueous fluids is quite slow within this horizon. Horizons B and B′ are also coarse-grained strata that appear to contain a relatively large amount of gas hydrate where they are present within the GHSZ and free gas below the GHSZ. The BSR is present throughout the region, except for immediately beneath a carbonate pinnacle near the summit and a few places in the slope basin east of southern Hydrate Ridge. All occurrences of gas hydrate or gas hydrate proxies were located above the BSR; in no cases were they unequivocally observed below it (Tréhu et al., 2004a).

The assumption that gas hydrate is approximately in thermodynamic equilibrium has led to the use of the BSR as a proxy for determining subsurface temperature, with deviations from the regional conductive temperature gradient interpreted to indicate heat transport by advection of pore water (e.g., Yamano et al., 1982; Zwart et al., 1996; Pecher et al., 2001; Tréhu et al., 2003; Wood et al., 2002). Whether gas hydrate in marine sediments is in thermodynamic equilibrium, however, has been a subject of some discussion. For example, Ruppel (1997, 2000) concluded that the observed base of gas hydrate stability, as defined by the BSR, is 0.5°–2.9°C colder than predicted beneath the Blake Ridge and attributed this to inhibition of gas hydrate formation by capillary forces. Other possible explanations for apparent mismatches between the temperature field and observations of BSR depth include temporal changes in the position of the stability boundary resulting
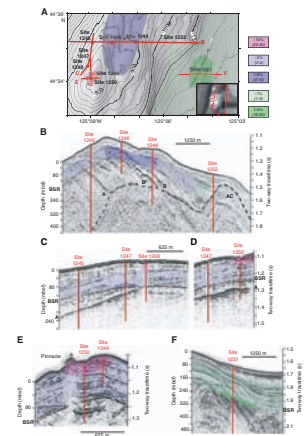
from sea level and ocean temperature changes that occur faster than the system can reequilibrate (Ruppel, 2000) and in situ departures from the assumed pore water chemistry or gas composition (Andreeson et al., 2000). Results from drilling at northern Hydrate Ridge during ODP Leg 146 were ambiguous, with some authors reporting that the BSR is shallower than predicted by measured in situ temperatures (Davis et al., 1995) and others concluding that it was in thermodynamic equilibrium (Brown et al., 1996).

The objective of this paper is to discuss and interpret in situ temperature measurements made during Leg 204 at southern Hydrate Ridge (Fig. F1A). Prior to Leg 204, an initial estimate of the temperature gradient in the region imaged by a 3-D seismic site survey was made based on the observed traveltime to the BSR assuming constant seafloor temperature, sediment velocity, and thermal conductivity. This exercise indicated the possibility that the thermal gradient, and consequently heat flow, might vary by as much as a factor of two between the summit and the slope basin to the east. Grevemeyer and Villinger (2001), however, reviewed all ODP data acquired from gas hydrate–bearing sites prior to Leg 204 and concluded that the uncertainty in heat flow estimates derived from BSR data can be as large as 50% unless high-quality in situ measurements are available. Although a map of regional heat flow calculated from the traveltime to the BSR observed in the 3-D seismic study showed apparent variations in heat flow of as much as a factor of two (Bangs et al., 2001), these variations could be accounted for by reasonable variations in seafloor temperature and seismic velocity. The results of the study presented in this paper, which include predicted methane hydrate stability limits calculated for measured pore water salinity and BSR depths constrained by vertical seismic profiles, confirm that no significant lateral variations in heat flow are needed to explain the data.

# INSTRUMENTATION

During Leg 204, 56 in situ temperature measurements were made using the Advanced Piston Corer Temperature (APCT) tool, which sits on the cutting shoe of the advanced piston corer (APC); 21 measurements were made with the Davis-Villinger Temperature-Pressure Probe (DVTPP); and six measurements were made with the Davis-Villinger Temperature Probe (DVTP) (Table T1). All but two of the APCT runs yielded good-quality data, but only about half of the DVTP and DVTPP runs did. The more variable quality of the DVTP and DVTPP data is due in large part to the fact that these tools are generally run deeper in the hole, where there is a greater probably of hitting lithified sediments that crack when the probe is inserted. They do provide, however, the only opportunity to obtain in situ temperature data at depths too great for the APCT, which was generally 200 mbsf for Leg 204. All of the temperature time series data from which in situ temperatures were derived are shown in the individual site chapters in Tréhu, Bohrmann, Rack, Torres, et al. (2003).

The APCT fits directly into the cutting shoe on the APC and can therefore be used to measure sediment temperatures during regular piston coring. Descriptions of the tool and of the principles behind analysis of the data it acquires can be found in Pribnow et al. (2000), Graber et al. (2002), and references therein. The only modification to normal APC procedures required to obtain temperature measurements is to

hold the corer in place for ~10 min after cutting the core. During this time, the APCT logs temperature data on a microprocessor contained within the instrument as it approaches equilibrium with the in situ temperature of the sediments. Following deployment, the data are downloaded for processing. The tool can be preprogrammed to record temperatures at a range of sampling rates. A sampling rate of 10 s was used during Leg 204. Figure F2A shows an annotated history of a typical APCT run. A typical measurement consists of a mudline temperature record lasting 10 min for the first deployment in each borehole and 2 min on subsequent runs. This is followed by a pulse of frictional heating when the piston is fired, a period of thermal decay that is monitored for at least 10 min, and a frictional pulse upon removal of the corer. Because of the long time needed for temperature reequilibration, the inferred in situ temperature can be several degrees lower than the measured temperature just before the tool is extracted.

The DVPT and DVTPP require dedicated runs. Temperature measurements made using the DVTP are described in detail by Davis et al. (1997) and summarized by Pribnow et al. (2000) and Graber et al. (2002). The DVTPP is a modified DVTP that also measures in situ pressure and was used previously during ODP Legs 190 and 201. The probe is conical and has two thermistors; the first is located 1 cm from the tip of the probe and the other 12 cm above the tip. For the DVTPP, the data stream from the upper thermistor is replaced by the pressure measurements. Because the time constant for pressure is expected to be longer, the DVTPP is held for at least 40 min in the formation. In this paper, we discuss only the temperature data from the DVTPP. Pressure records are being analyzed by M. Heeseman (pers. comm., 2002).

## ESTIMATION OF IN SITU TEMPERATURE

For the APCT, the in situ temperature was derived from the data using TFIT, a program developed by Keir Becker and James Craig based on the algorithm of Horai and von Herzen (1985). For the DVTP, data were analyzed using CONEFIT, developed by Davis et al. (1997). In both cases, the decay of an initial pulse of heat is modeled as a function of the geometry of the probe and the thermal conductivity, diffusivity, and heat capacity of the probe and of the surrounding sediment. The models are based on one-dimensional analytical solutions to the problem that ignore effects of variations in thermal properties of the material surrounding the probe, along-axis heat conduction, and the finite time for the initial frictional heat pulse. Impulse responses are calculated (Fig. F2B) for different values of sediment thermal conductivity, assuming that the relationship between thermal conductivity, thermal diffusivity, and heat capacity is known (Hyndman et al., 1979). The in situ temperature ($T_o$) can be estimated by finding the combination of initial frictional heat ($T_f$), thermal conductivity ($k$), and start time ($t_s$) that minimizes the misfit between the data and the observations. Hartmann and Villinger (2002) discuss the limitations of this simplified model and argue that variations in $t_s$, expressed as a time shift relative to the observed penetration time $t_p$ (Fig. F2), compensate for inadequacies in the theoretical model during the initial rise and decay of the frictional heating pulse. Because of inadequacies in the model, it is also important to carefully chose the data window used to estimate $T_o$. Pribnow et al. (2000) examined the effect of varying the start and stop
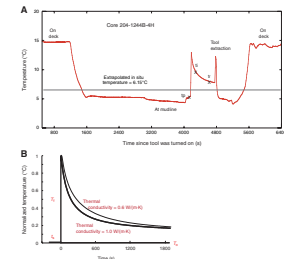
times of this window. If $t_i$ is too close to $t_p$, the misfit increases because of the inadequacy of the model for explaining details of the initial thermal decay; for $t_e$ too large, the misfit increases as unmodeled effects of along-axis heat conduction become important.

## Instrument Calibration

Doubts concerning instrument calibration were a significant source of uncertainty during Leg 204. Although the precision of the sensors used in the ODP temperature tools is nominally better than 0.01°C, leading to robust measurements of the temperature gradient if the same tool is used for all measurements, the absolute value of temperature is known to only ±0.10°C because of uncertainties in instrument calibration. The APCT tools were calibrated while at sea by submerging them in an ice-water bath for at least 30 min. Apparent equilibrium temperatures for the different APCT tools varied from –2.5° to +1.0°C (Shipboard Scientific Party, 2003b), suggesting significant calibration offsets. The poor calibration of the sensors was surprising because the need for good instrument calibration had been discussed before the cruise. The DVTP and DVTPP instruments were calibrated by comparing measurements made with those tools with APCT measurements made at approximately the same depth at the same site. All calibration factors determined by the empirical comparisons are given in Table T1.

The ice-water calibration experiment was done in response to observation of a strongly nonlinear temperature profile at Site 1246, which contrasted with linear temperature gradients that had been observed at sites visited earlier during the leg. Closer examination of the data indicated an apparent decrease in bottom water temperature of ~2.5°C between the time when the probe penetrated the sediment and the time when it was extracted during collection of Core 204-1246B-5H (Fig. F3). APCT measurements immediately before and after this measurement, on Cores 204-1246B-3H and 7H, showed similar temperatures before and after sampling the subsurface but were offset by this amount (Fig. F3). Such an abrupt change in bottom water temperature in such a short time is highly unlikely. When APCT12 was tested in the ice-water bath after completion of coring at Site 1246, it indicated a temperature of –2.50°C. At this point, we retired APCT12 and started using APCT11, which had one of the smallest calibration offsets during the ice-water calibration test (–0.51°C). We concluded that the temperature sensor on APCT12 underwent a sudden, negative "jump" in calibration. Such behavior of the APCT temperature probes has not previously been documented, as far as we know. Further evidence for this jump is provided by analysis of in situ temperatures recorded at Site 1244, where four measurements were taken with APCT12 and six were taken with APCT11. When linear temperature profiles are using data from only one tool, similar slopes are obtained, but the intercepts are offset by 0.58°C (Shipboard Scientific Party, 2003b). We conclude from this exercise that APCT12 was accurate to better than 0.1°C prior to the change in calibration.

Often the calibration of downhole temperature tools is confirmed by measuring the bottom water temperature and comparing that value to other measurements of bottom water temperature in the region (e.g., Pribnow et al., 2000; Shipboard Scientific Party, 2003a). At the water depths encountered during Leg 204, however, peak to peak tidal variations of as much as 0.3°C (R. Collier, unpubl. data) make this approach unreliable.



**F3.** Water temperatures, p. 17.
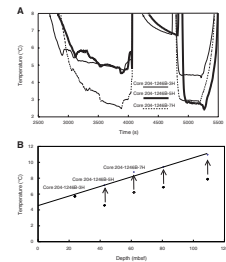
## Uncertainty in Thermal Conductivity

One of the primary sources of uncertainty in this analysis is the in situ thermal conductivity (Villinger and Davis, 1987; Davis et al., 1990). Hartmann and Villinger (2002) showed that there is a trade-off between the best-fit in situ temperature and thermal conductivity. This trade-off is shown in Figure F4A, where the misfit as a function of $t_s$ and thermal conductivity usually shows a well-defined valley within which $T_o$ increases as thermal conductivity decreases. An independent measure of thermal conductivity is generally used to allow only realistic thermal conductivities. Similarly, a better understanding of factors leading to nonzero $t_s$ and to variations in $T_f$ could potentially be used to help constrain $T_o$.

With shallow probes, the in situ conductivity is generally measured directly by modeling the temperature decay resulting from a known input of heat (Lister, 1970; Villinger and Davis, 1987) For downhole temperature tools in boreholes, however, this is not practical (H. Villinger, pers. comm., 2005), and in situ thermal conductivity is estimated based on shipboard measurements of thermal conductivity on core samples using the needle probe method of Von Herzen and Maxwell (1959), corrected to in situ pressure and temperature conditions (Ratcliffe, 1960; Hyndman et al., 1974). Whereas individual measurements made with this technique are often very precise, there can be considerable variation between measurements made meters apart, especially in turbidite-rich sediments from continental margins like those drilled during Leg 204. Moreover, gas expansion during core recovery and/or intrusion of drilling mud into the core also affect the measurements on core samples, leading to underestimated thermal conductivity. On the other hand, if a measurement were made in sediments containing a significant amount of free gas or in a massive gas hydrate lens, the in situ thermal conductivity would be lower than the thermal conductivity measured on recovered sediment cores. This may explain the anomalously low thermal conductivity of ~0.5 W/(m·K) indicated by the minimum misfit for the APCT measurement made at the base of Core 204-1249F-8H (Fig. F4A). In situ electrical resistivity measured with LWD data (Lee and Collett, this volume) was also very low at 40 mbsf at this site.

Thermal conductivities measured on core samples during Leg 204 are shown to the left of the graphs of temperature as a function of depth in Figures F5, F6, F7, F8, and F9. For Site 1244, both the uncorrected and corrected values are shown; only corrected data are shown for the other sites. For the relatively shallow water and subseafloor depths sampled during Leg 204, this correction is <0.05 W/(m·K). The thermal conductivity measurements show considerable scatter, and with the exception of the upper ~100 m at Sites 1251 and 1250, any systematic change in thermal conductivity with depth is not resolved or is small enough that it can be neglected. For these sites, the average thermal conductivity (Table T2) was used to extrapolate the data to in situ temperature and to calculate heat flow. For Sites 1251 and 1252, a two-layer model was used. Averages and standard deviations of thermal conductivity are given in Table T2. The uncertainty in $T_o$ resulting from uncertainty in the thermal conductivity (Fig. F4) is estimated to be generally less than ±0.15°C.
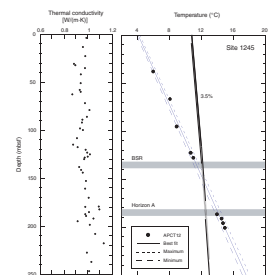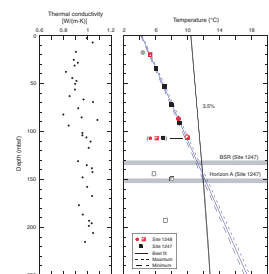
F4. Temperature and thermal conductivity, p. 18.
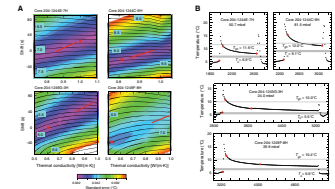
F5. Thermal conductivity, Site 1244, p. 19.
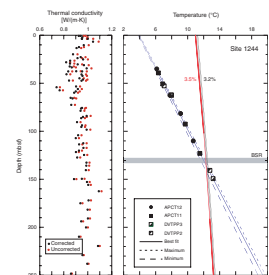
F6. Thermal conductivity, Site 1245, p. 20.

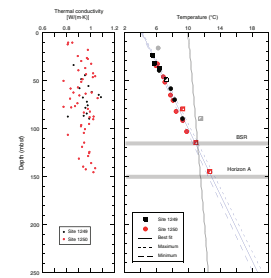F7. Thermal conductivity, Sites 1247 and 1248, p. 21.

# RESULTS

Temperature gradients were calculated for all sites. Only high-quality data that showed frictional pulses both on insertion and extraction were used to define the in situ temperature profiles shown in Figures F5, F6, F7, F8, and F9. If a secondary frictional disturbance was observed during the reequilibration period, extrapolation for $T_o$ was based only on data recorded prior to the disturbance. The plotted symbols have dimensions of 0.6°C by 4 km, similar to the estimated uncertainties in temperature and depth. Data that were excluded from the determination of the best-fit thermal gradient are shown in gray. All excluded data showed anomalous behavior (e.g., indications that the probe had not penetrated the seafloor, apparent cooling by borehole fluid prior to extraction, or multiple secondary frictional pulses). Because of possible temporal changes in the bottom water temperature resulting from tides, seasons, and longer period changes in bottom water temperature, seafloor temperatures were not used when calculating the thermal gradient.

The slope, intercept, and associated standard errors for each site are given in Table T2, as is the apparent data uncertainty implied by the misfit of the measurements to a linear model. For reasons discussed below, subsets of the data at a given site or combinations of data from two different sites are sometimes shown. In all cases, the apparent misfit is smaller than our estimated data uncertainty of ±0.3°C, indicating that a linear model is appropriate for these data. For several sites for which five or fewer samples are available, the apparent misfit is much smaller, indicating that the statistics for these sites are not reliable and that the uncertainty in the slope and intercepts are larger than indicated.

The average thermal conductivity and heat flow are also given in Table T2. Uncertainties in the heat flow include uncertainties in the temperature gradient and in the thermal conductivity. Even though there appear to be significant differences among the thermal gradients (e.g., comparing Site 1244 [Fig. F5] on the eastern flank and Site 1245 [Fig. F6] on the western flank of southern Hydrate Ridge), these are compensated by differences in the thermal conductivity. The differences in thermal conductivity are consistent with lithologic differences, with higher thermal conductivity measured on average in the turbidite-rich slope basin sediments of the eastern flank. The lowest thermal conductivities, as well as the only clear systematic depth dependence of thermal conductivity, are observed in the very young, rapidly deposited sediments of the slope basin located east of southern Hydrate Ridge (Fig. F9). The apparent heat flow through this basin also appears to be slightly lower than the heat flow through southern Hydrate Ridge, consistent with the high sedimentation rate.

The heat flow at southern Hydrate Ridge is similar to the heat flow of 53 ± 3 mW/m² determined at ODP Site 892 beneath northern Hydrate Ridge (Shipboard Scientific Party, 1994) and lower than the heat flow of 71 mW/m² reported for the Site 892 circulation obviation retrofit kit (CORK) (Davis et al., 1995). Davis et al. (1995) attributed the difference between heat flow determined from measurements made during Leg 146 and heat flow determined from the CORK to transient fluid flow along a fault and location of many of the measurements in the footwall of the fault. This explanation cannot be invoked for southern Hydrate Ridge, where the low heat flow is regionally pervasive.

**F8.** Thermal conductivity, Sites 1249 and 1250, p. 22.

**F9.** Thermal conductivity, Sites 1251 and 1252, p. 23.
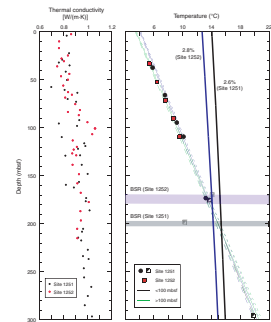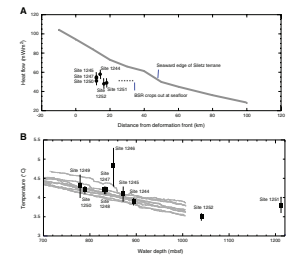
**T2.** Thermal gradients, p. 26.

The heat flow at southern Hydrate Ridge is only ~60% of what is predicted by a thermal model (Fig. F10A) that includes the age and dip of the subducting plate and the thickness of the overlying accretionary complex (Oleskevich et al., 1999). A similar mismatch between the heat flow obtained from borehole temperatures at Site 889 and that obtained from tectonic modeling constrained by shallow observations has been noted for the accretionary complex offshore Vancouver Island, where the regional heat flow regime is better constrained than off Oregon (Davis et al., 1990; Hyndman and Davis, 1992; Hyndman et al., 1993; Oleskevich et al., 1999) and has been attributed to the combined effects of sediment thickening and fluid expulsion. A tectonostratigraphic reconstruction of southern Hydrate Ridge suggests that the low thermal gradient here may result from the cooling effects of underplating rather than sediment thickening. The tectonic implications of the low apparent heat flow recorded during Legs 146 and 204 will be discussed in more detail in a future manuscript that includes constraints from Integrated Ocean Drilling Project Expedition 311 to the Vancouver acccretionary complex.

The seafloor intercept of the best-fit linear solution was compared to bottom water temperatures measured by concentration/temperature/depth recorders (CTDs) (Fig. F10B). The seafloor intercept falls within the expect range of temperatures for all sites except for Sites 1246 and 1251. The slope for Site 1246 is poorly constrained because of the small number of measurements and the possible tool instability documented in Figure F3. The intercept for Site 1251 obtained using all data is probably biased by the fact that the thermal conductivity is not constant; moreover, we do not have data from this region for water depths <1000 m. This correspondence indicates that the subsurface thermal profile is in thermal equilibrium with the seafloor and provides further evidence for a dominantly conductive thermal regime. If the anomalously low thermal gradient was due to distributed dewatering of the accretionary complex, the projected seafloor temperature implied by the observations would be higher than the observed seafloor temperature (Davis et al., 1990).

Because measurements were made at both sites within 10 m of the seismically determined BSR, the temperature at this boundary is well constrained. At all sites, the predicted depth to the BSR is slightly deeper than the observed BSR depth, although this trend is only marginally significant. This difference is much smaller than the offset reported for the Blake Ridge, where the BSR may be 50–100 m shallower than predicted by in situ temperatures (Ruppel, 1997). At the Blake Ridge, the preferred explanation for the offset is inhibition of gas hydrate formation by capillary forces in fine-grained clay sediments. This process may also be occurring at Hydrate Ridge to produce an offset of 0–10 m between the observed and predicted temperature at the BSR.

Perhaps surprisingly, no thermal perturbation was observed in the vicinity of Horizon A at Site 1245. Horizon A is a 2- to 4-m-thick, relatively coarse grained, volcanic ash–rich horizon that contains free gas at a saturation high enough to lead to high gas pressure and free gas migration (Tréhu et al., 2004b). This observation is supported by four closely spaced measurements that were obtained at 185–200 mbsf in Hole 1245C (Fig. F6), which do not show any temperature anomaly indicative of heat transport through fluid migration. We interpret these observations to indicate that fluid transport is in the free gas phase, with very little flow of aqueous pore fluid, and that heat transported by the free gas is not effectively transferred to the surrounding sediments.

**F10.** Heat flow, p. 24.

Also surprising is the observation that no significant departures from the regional thermal gradient are observed at Sites 1248, 1249, and 1250, which were located at the summit where massive gas hydrate in the upper 20–30 mbsf shows the fingerprint of migrated thermogenic gas. Rapid (as much as 1000 cm/yr) but temporally variable fluid flow through the seafloor (Tryon et al., 2002) and local high geothermal gradients in the upper meter beneath the seafloor (Tréhu et al., unpubl. data) have been documented here. These observations can be reconciled with the downhole temperature data by invoking shallow circulation of aqueous pore fluid that is confined to the upper tens of meters.

# CONCLUSIONS

1. Subsurface measurements of in situ temperature are generally consistent with a conductive temperature profile. Variations in the apparent thermal gradient between sites are due primarily to differences in the average thermal conductivity of different sedimentary facies. Regional heat flow is ~54 mW/m². Heat flow may be slightly depressed in the slope basin east of southern Hydrate Ridge (~49 mW/m² at Site 1251) and slightly elevated in a region of pervasive shallow normal faults northeast of the summit (~58 mW/m² at Site 1244), but these differences are within the measurement uncertainties. Heat flow is only ~60% of the heat flow predicted by a model that included the age and velocity of the subducting plate and the thickening of the accreted sediments.

2. The seafloor intercept of the geothermal gradient defined by the borehole temperature estimates is generally consistent with the expected seafloor temperature, indicating regional thermal equilibrium to a depth of at least 300 mbsf.

3. The depth of the seismic BSR corresponds to the predicted depth to the methane hydrate stability boundary calculated for hydrostatic pressure and the measured in situ pore water salinity to within the uncertainty in the measurements. A small systematic shallowing of the BSR by 0–10 m is possible, indicating that inhibition of gas hydrate formation in these fine-grained sediments may occur.

4. Anomalous solutions for in situ temperatures taken at depths above 50 mbsf near the summit may reflect the effect of low in situ thermal conductivity in the immediate vicinity of the temperature probe. This may result either from perturbations to the local temperature field because of dissociation and reformation of gas hydrate or to low in situ thermal conductivity resulting from the presence of massive hydrate and/or of free gas in the sediments. Better calibrated measurements, longer time series, and more complete models are needed to better understand the implications of these anomalous observations.

5. No thermal anomaly is associated with Horizon A, a coarse-grained stratigraphic horizon that is the major conduit transporting gas to the summit vents, indicating that fluid flow is episodic and not recent or that methane is transported to the summit as free gas.

6. The dominance of a conductive thermal gradient at the summit, where gas migration is indicated based on massive hydrate in the shallow subsurface, plumes of bubbles venting to the seafloor,

and geochemical fingerprints of thermogenic gas, indicates the importance of two-phase flow for understanding the behavior of this gas hydrate system.

# ACKNOWLEDGMENTS

# REFERENCES

Andreeson, K., Mienert, J., Bryn, P., and Singh, S.C., 2000. A double gas-hydrate related bottom simulating reflector at the Norwegian continental margin. *In* Holder, G.D., and Bishnoi, P.R. (Eds.), *Gas Hydrates: Challenges for the Future.* Ann. N. Y. Acad. Sci., 912:126–135.

Bangs, N.L., Tréhu, A.M., and Sen, M., 2001. Mapping methane-rich fluid systems within southern Hydrate Ridge with high-resolution 3-D seismic reflection data. *Eos, Trans. Am. Geophys. Union,* 82:OS12B-0422. (Abstract)

Bangs, N.L.B., Musgrave, R.J., and Tréhu, A.M., 2005. Upward shifts in the southern Hydrate Ridge gas hydrate stability zone following postglacial warming, offshore Oregon. *J. Geophys. Res.,* 110(B3):B03102. doi:10.1029/2004JB003293

Brown, K.M., Bangs, N.L., Froelich, P.N., and Kvenvolden, K.A., 1996. The nature, distribution, and origin of gas hydrate in the Chile triple junction region. *Earth Planet. Sci. Lett.,* 139:471–483. doi:10.1016/0012-821X(95)00243-6

Davis, E.E., Becker, K., Wang, K., and Carson, B., 1995. Long-term observations of pressure and temperature in Hole 892B, Cascadia accretionary prism. *In* Carson, B., Westbrook, G.K., Musgrave, R.J., and Suess, E. (Eds.), *Proc. ODP, Sci. Results,* 146 (Pt. 1): College Station, TX (Ocean Drilling Program), 299–311.

Davis, E.E., Hyndman, R.D., and Villinger, H., 1990. Rates of fluid expulsion across the northern Cascadia accretionary prism: constraints from new heat flow and multichannel seismic reflection data. *J. Geophys. Res.,* 95:8869–8889.

Davis, E.E., Villinger, H., MacDonald, R.D., Meldrum, R.D., and Grigel, J., 1997. A robust rapid-response probe for measuring bottom-hole temperatures in deep-ocean boreholes. *Mar. Geophys. Res.,* 19:267–281. doi:10.1023/A:1004292930361

Graber, K.K., Pollard, E., Jonasson, B., and Schulte, E. (Eds.), 2002. Overview of Ocean Drilling Program Engineering Tools and Hardware. *ODP Tech. Note,* 31 [Online]. Available from World Wide Web: <http://www-odp.tamu.edu/publications/tnotes/tn31/INDEX.HTM>. [Cited 2005-02-03]

Grevemeyer, I., and Villinger, H., 2001. Gas hydrate stability and the assessment of heat flow through continental margins. *Geophys. J.,* 145:447–460.

Hartmann, A., and Villinger, H., 2002. Inversion of marine heat flow measurements by expansion of the temperature decay function. *Geophys. J. Int.,* 148:628–636. doi:10.1046/j.1365-246X.2002.01600.x

Horai, K., and Von Herzen, R.P., 1985. Measurement of heat flow on Leg 86 of the Deep Sea Drilling Project. *In* Heath, G.R., Burckle, L.H., et al., *Init. Repts. DSDP,* 86: Washington (U.S. Govt. Printing Office), 759–777.

Hyndman, R.D., and Davis, E.E., 1992. A mechanism for the formation of methane hydrate and seafloor bottom-simulating reflectors by vertical fluid expulsion. *J. Geophys. Res.,* 97:7025–7041.

Hyndman, R.D., Erickson, A.J., and Von Herzen, R.P., 1974. Geothermal measurements on DSDP Leg 26. *In* Davies, T.A., Luyendyk, B.P., et al., *Proc. DSDP, Init. Repts.,* 26: Washington (U.S. Govt. Printing Office), 451–463.

Hyndman, R.D., Davis, E.E., and Wright, J.A., 1979. The measurement of marine geothermal heat flow by a multipenetration probe with digital acoustic telemetry and in-situ thermal conductivity. *Mar. Geophys. Res.,* 4:181–205. doi:10.1007/BF00286404

Hyndman, R.D., Wang, K., Yuan, T., and Spence, G.D., 1993. Tectonic sediment thickening, fluid expulsion, and the thermal regime of subduction zone accretionary prisms: the Cascadia margin off Vancouver Island. *J. Geophys. Res.,* 98:21865–21876.

Lister, C.R.B., 1970. Heat flow west of the Juan de Fuca Ridge. *J. Geophys. Res.,* 75:2648–2654.

Milkov, A.V., Dickens, G.R., Claypool, G.E., Lee, Y-J., Borowski, W.S., Torres, M.E., Xu, W., Tomaru, H., Trehu, A.M., and Schultheiss, P., 2004. Co-existence of gas

hydrate, free gas, and brine within the regional gas hydrate stability zone at Hydrate Ridge (Oregon margin): evidence from prolonged degassing of a pressurized core. *Earth Planet. Sci. Lett.,* 222:829–843. doi:10.1016/j.epsl.2004.03.028

Oleskevich, D.A., Hyndman, R.D., and Wang, K., 1999. The updip and downdip limits to great subduction earthquakes: thermal and structural models of Cascadia, south Alaska, SW Japan and Chile. *J. Geophys. Res.,* 104:14965–14991. doi:10.1029/1999JB900060

Pecher, I.A., Kukowski, N., Ranero, C.R., and von Huene, R., 2001. Gas hydrates along the Peru and Middle America Trench system. *In* Paull, C.K., and Dillon, W.P. (Eds.), *Natural Gas Hydrates: Occurence, Distribution, and Detection.* Geophys. Monogr., 124:257–271.

Pribnow, D.F.C., Kinoshita, M., and Stein, C.A., 2000. Thermal data collection and heat flow recalculations for ODP Legs 101–180. Institute for Joint Geoscientific Research, GGA, Hanover, Germany, 0120432. Available from World Wide Web: <http://www-odp.tamu.edu/publications/heatflow/ODPReprt.pdf> [Cited 2005-02-03]

Ratcliffe, E.H., 1960. The thermal conductivities of ocean sediments. *J. Geophys. Res.,* 65:1535–1541.

Ruppel, C., 1997. Anomalously cold temperatures observed at the base of the gas hydrate stability zone on the U.S. Atlantic passive margin. *Geology,* 25:699–702. doi:10.1130/0091-7613(1997)025<0699:ACTOAT>2.3.CO;2

Ruppel, C., 2000. Thermal state of the gas hydrate reservoir. *In* Max, M.D. (Ed.), *Natural Gas Hydrate in Oceanic and Permafrost Environments:* Dordrecht (Kluwer Academic Publishers), 29–42.

Shipboard Scientific Party, 1994. Site 892. *In* Westbrook, G.K., Carson, B., Musgrave, R.J., et al., *Proc. ODP, Init. Repts.,* 146 (Pt. 1): College Station, TX (Ocean Drilling Program), 301–378.

Shipboard Scientific Party, 2003a. Explanatory notes. *In* Morris, J.D., Villinger, H.W., Klaus, A., *Proc. ODP, Init. Repts.,* 205, 1–76 [CD-ROM]. Available from: Ocean Drilling Program, Texas A&M University, College Station TX 77845-9547, USA. [HTML]

Shipboard Scientific Party, 2003b. Site 1244. *In* Tréhu, A.M, Bohrmann, G., Rack, F.R., Torres, M.E., et al., *Proc. ODP, Init. Repts.,* 204, 1–132 [CD-ROM]. Available from: Ocean Drilling Program, Texas A&M University, College Station TX 77845-9547, USA. [HTML]

Sloan, E.D., 1998. *Clathrate Hydrates of Natural Gases* (2nd ed.): New York (Marcel Dekker).

Torres, M.E., Wallmann, K., Tréhu, A.M., Bohrmann, G., Borowski, W.S., and Tomaru, H., 2004. Gas hydrate growth, methane transport, and chloride enrichment at the southern summit of Hydrate Ridge, Cascadia margin off Oregon. *Earth Planet. Sci. Lett.,* 226:225–241. doi:10.1016/j.epsl.2004.07.029

Tréhu, A.M., Bohrmann, G., Rack, F.R., Torres, M.E., et al., 2003. *Proc. ODP, Init. Repts.,* 204 [CD-ROM]. Available from: Ocean Drilling Program, Texas A&M University, College Station TX 77845-9547, USA. [HTML]

Tréhu, A.M., Flemings, P.B., Bangs, N.L., Chevallier, J., Gràcia, E., Johnson, J.E., Liu, C.S., Liu, X., Riedel, M., and Torres, M.E., 2004a. Feeding methane vents and gas hydrate deposits at south Hydrate Ridge. *Geophys. Res. Lett.,* 31:L23310. doi:10.1029/2004GL021286

Tréhu, A.M., Lin, G., Maxwell, E., and Goldfinger, C., 1995. A seismic reflection profile across the Cascadia subduction zone offshore central Oregon: new constraints on methane distribution and crustal structure. *J. Geophys. Res.,* 100:15101–15116. doi:10.1029/95JB00240

Tréhu, A.M., Long, P.E., Torres, M.E., Bohrmann, G., Rack, F.R., Collett, T.S., Goldberg, D.S., Milkov, A.V., Riedel, M., Schultheiss, P., Bangs, N.L., Barr, S.R., Borowski, W.S., Claypool, G.E., Delwiche, M.E., Dickens, G.R., Gracia, E., Guerin, G., Holland, M., Johnson, J.E., Lee, Y.-J., Liu, C.-S., Su, X., Teichert, B., Tomaru, H., Vanneste, M., Watanabe, M., and Weinberger, J.L., 2004b. Three-dimensional distribution of gas

hydrate beneath southern Hydrate Ridge: constraints from ODP Leg 204. *Earth Planet. Sci. Lett.,* 222(3–4):845–862. **doi:10.1016/j.epsl.2004.03.035**

Tréhu, A.M., Stakes, D.S., Bartlett, C.D., Chevallier, J., Duncan, R.A., Goffredi, S.K., Potter, S.M., and Salamy, K.A., 2003. Seismic and seafloor evidence for free gas, gas hydrates, and fluid seeps on the transform margin offshore Cape Mendocino. *J. Geophys. Res.,* 108. **doi:10.1029/2001JB001679**

Tryon, M.D., Brown, K.M., and Torres, M.E., 2002. Fluid and chemical flux in and out of sediments hosting methane hydrate deposits on Hydrate Ridge, OR. II: Hydrological processes. *Earth Planet. Sci. Lett.,* 201(3–4):541–557. **doi:10.1016/S0012-821X(02)00732-X**

Villinger, H., and Davis, E.E., 1987. A new reduction algorithm for marine heat flow measurements. *J. Geophys. Res.,* 92:12846–12856.

Von Herzen, R.P., and Maxwell, A.E., 1959. The measurement of thermal conductivity of deep-sea sediments by a needle-probe method. *J. Geophys. Res.,* 64:1557–1563.

Wood, W.T., Gettrust, J.F., Chapman, N.R., Spence, G.D., and Hyndman, R.D., 2002. Decreased stability of methane hydrates in marine sediments owing to phase-boundary roughness. *Nature (London, U. K.),* 420:656–660. **doi:10.1038/nature01263**

Yamano, M., Uyeda, S., Aoki, Y., and Shipley, T.H., 1982. Estimates of heat flow derived from gas hydrates. *Geology,* 10:339–343. **doi:10.1130/0091-7613(1982)10<339:EOHFDF>2.0.CO;2**

Zwart, G., Moore J.C., and Cochrane, G.R., 1996. Variations in temperature gradients identify active faults in the Oregon accretionary prism. *Earth Planet. Sci. Lett.,* 139:485–495. **doi:10.1016/0012-821X(95)00244-7**

**Figure F1. A.** Locations of sites drilled during Leg 204. Insert shows seafloor reflectivity at the summit, with the 800 m depth contour for reference. Overlay shows gas hydrate content of the sediment averaged from the seafloor to the BSR. Red lines show the location of seismic profiles. Numbers in parentheses in the legend represent gas hydrate content of the pore space averaged over the depth intervals shown in the seismic sections. See Tréhu et al. (2004a) for determinations of gas hydrate content. **B–F.** Seismic sections extracted from the 3-D seismic data. Reflections at Horizons A, B, and B′ and the bottom-simulating reflection (BSR) are discussed in the text. AC prepresents the top of older, highly deformed accretionary complex sediments that are overlain by uplifted and deformed slope basin sediments (see **Chevallier et al.,** this volume). (**Figure shown on next page.**)

**Figure F1.** (Caption shown on previous page.)
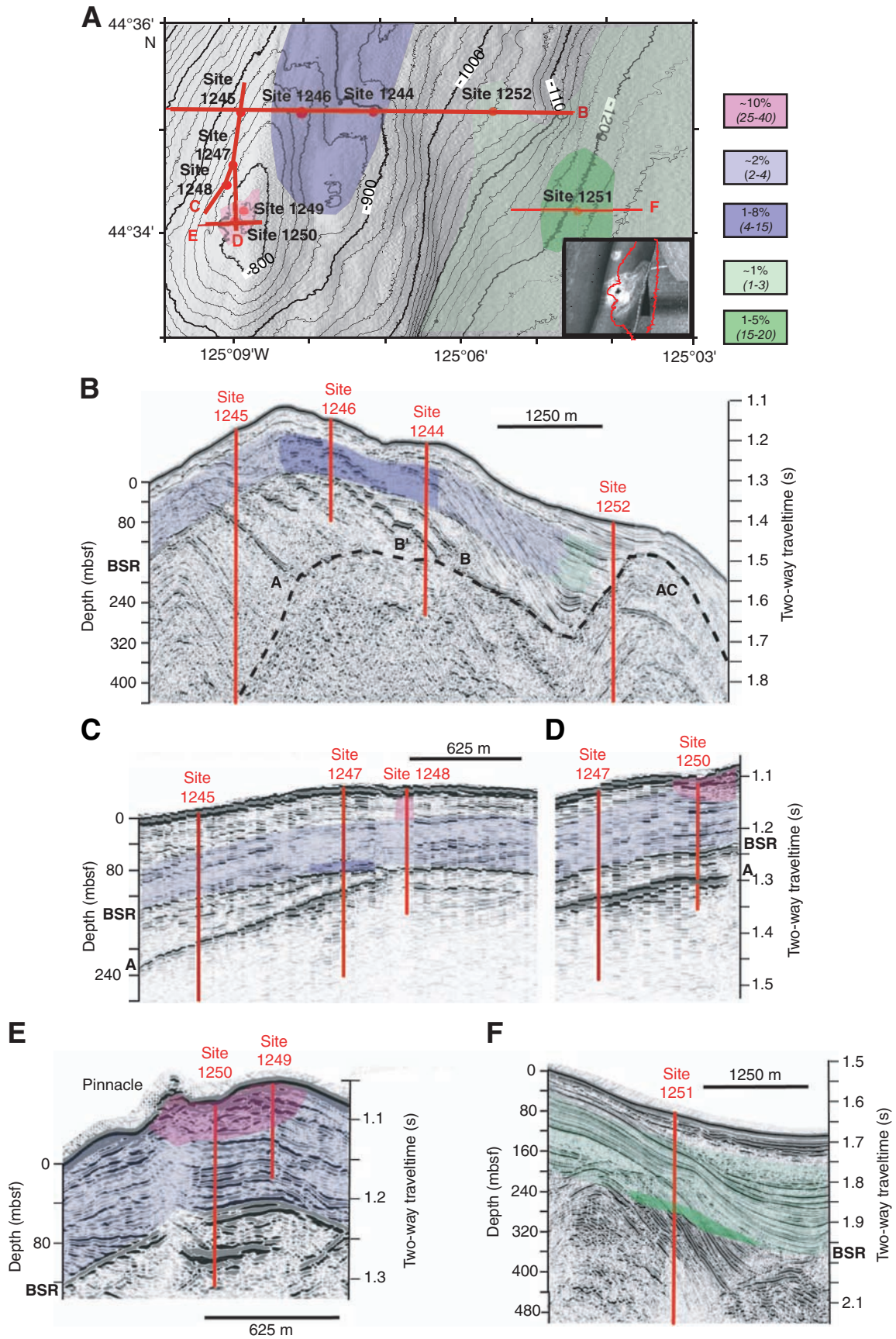
**Figure F2. A.** Example of the temperature history recorded by the APCT. In situ temperature is estimated based on the decay of the frictional heat pulse that occurs when the tool enters the sediments. A second frictional heat pulse when the tool is extracted indicates good coupling to the sediments. $t_p$, $t_i$, and $t_r$ represent data values picked by the user to indicate the time of tool penetration and the start and end time of the data window to model. Similar temperature histories are recorded for all of the tools used to measure in situ temperature during Leg 204. **B.** Impulse response for the APCT calculated using the algorithm of Horai and von Herzen (1985) as implemented in TFIT. This algorithm assumes that the instrument is a cylinder that is heated instantaneously to a temperature $T_f$ and that all heat flow is radial. The decay curve is a function of the geometry of the instrument and the thermal properties of the surrounding sediment. Decay curves are shown for two values of thermal conductivity, assuming that thermal diffusivity and heat capacity are simple functions of thermal conductivity. The in situ temperature, $T_o$, is estimated by finding the best fitting combination of $t_s$ (time shift of the impulse response relative to $t_p$), $T_f$, and thermal conductivity for a given data window.
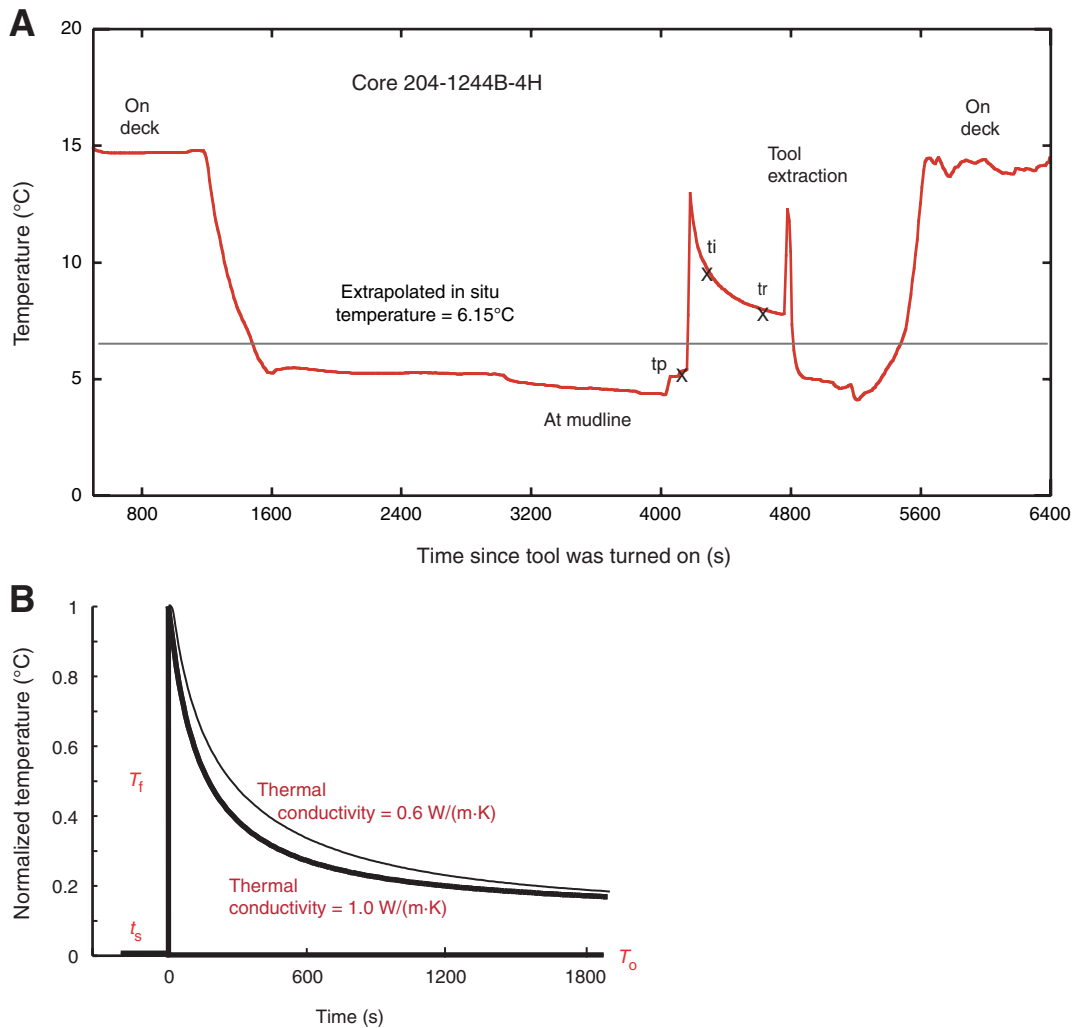
**Figure F3. A.** Water temperatures recorded during three consecutive runs of APCT12 at Site 1246. These observations show a rapid change in apparent bottom water temperature while a measurement was being made during acquisition of Core 204-1246B-5H. Such a rapid change is not likely and is interpreted to indicate a sudden "recalibration" of APCT12. We were not able to identify the source of the problem. **B.** The effect of shifting $T_o$ estimates made at Site 1246 to correct for the problem illustrated in A. APCT12 was retired after Site 1246 and replaced by APCT11.
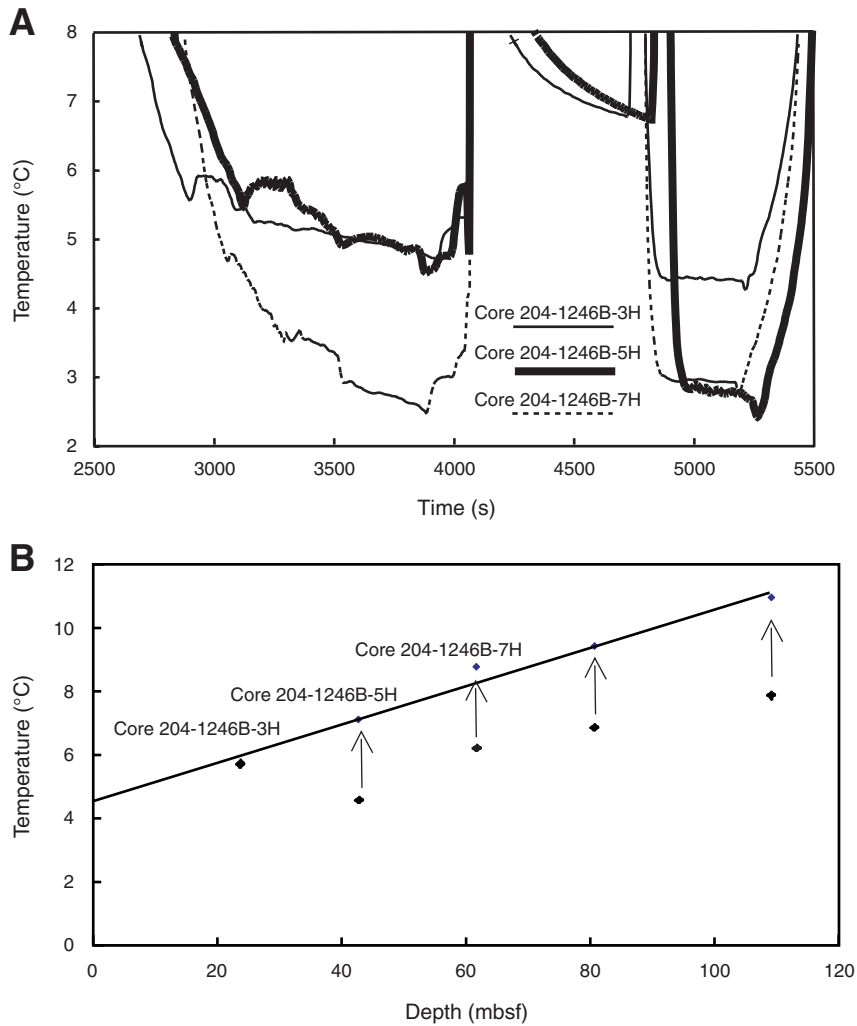
**Figure F4. A.** Trade-off between $t_s$ and thermal conductivity when determining $T_o$. Color represents the standard error of the solution. Contours represent best-fit $T_o$ in °C. Red dots show the minimum standard error. Red lines show the range of thermal conductivities measured in the cores. **B.** Data (black dots) and picked values for $t_p$, $t_i$, and $t_r$ (red dots). The optimum data window to fit was determined empirically and was consistent for all data. The best fit $T_o$ and the temperature at which gas hydrate is not stable at this depth ($T_{gh}$) are also shown. Stability boundaries determined using CSMHYD98 (Sloan, 1998) for the pore water salinity measured near the base of the gas hydrate stability zone. At shallow subseafloor depths near the summit, the local salinity at the measurement position may be higher, so $T_{gh}$ shown here is an upper limit. The initial frictional heating pulse raises the temperature above the temperature for gas hydrate stability in all cases.
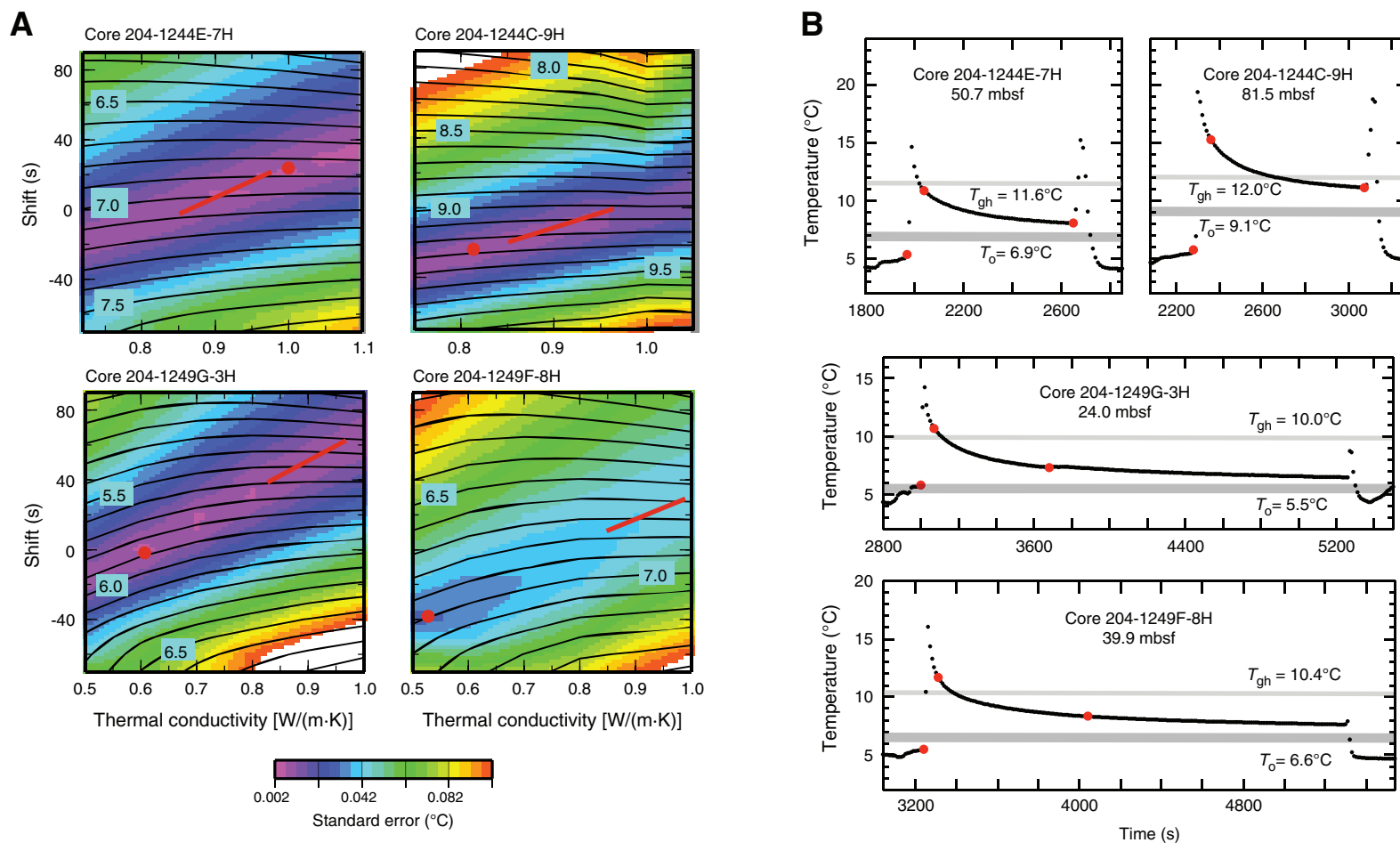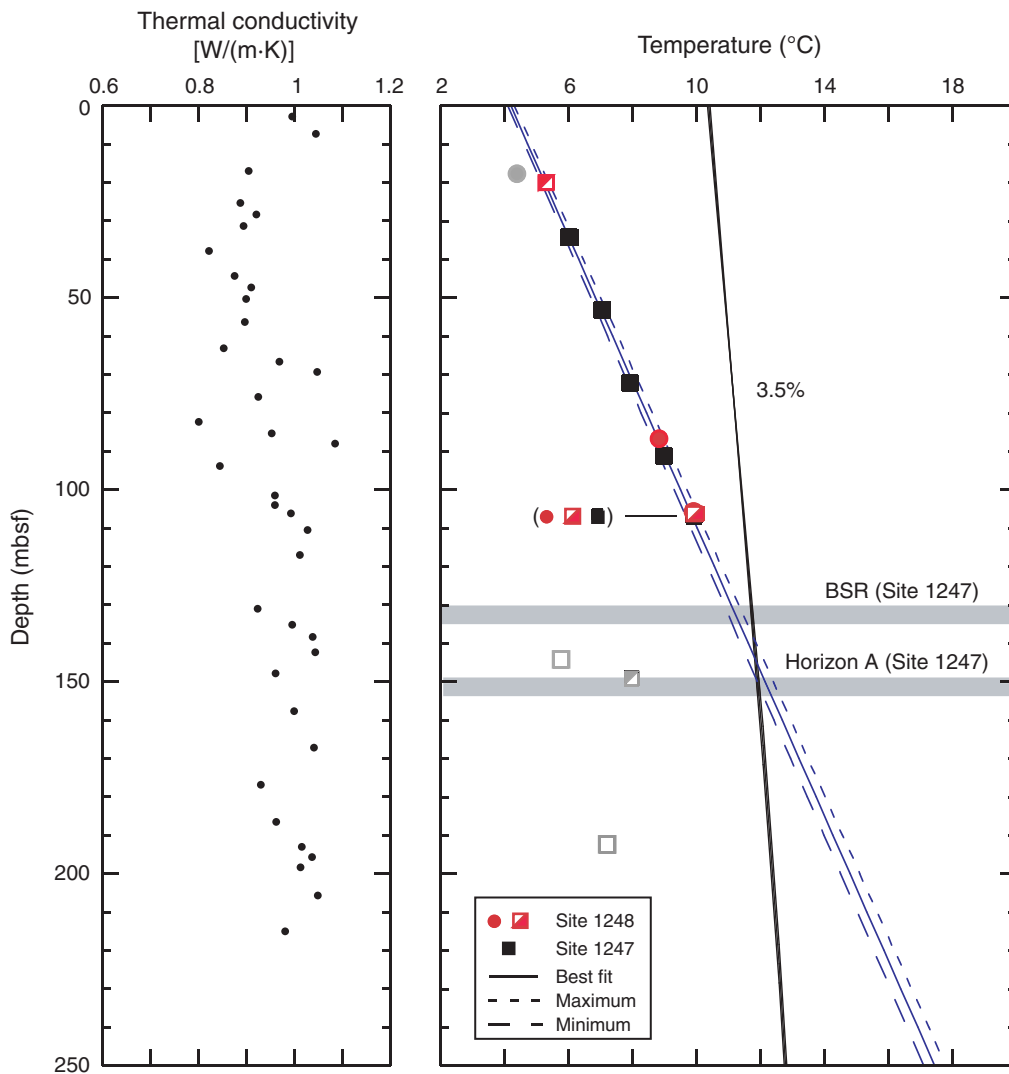
**Figure F5.** Thermal conductivity measured by the Davis-Villinger Temperature-Pressure Probe (DVTPP) and Advance Piston Corer Temperature (APCT) tools on recovered cores (Shipboard Scientific Party, 2003c) and $T_o$ plotted vs. depth at Site 1244. Each small symbol represents the average of three needle probe measurements. Open circles = thermal conductivity at ambient pressure and temperature in the laboratory; solid circles = data corrected to in situ conditions. All in situ temperature estimates have been corrected using the empirically determined calibration constants given in Table **T1,** p. 25. This site was important for determining these constants because of the large number of measurements made and the variety of tools used. Note that both DVTPP tools, which cannot be easily submerged in a water bath on the ship, were co-located with APCT tools at this site. Overlain on the data is the best-fit linear thermal gradient with uncertainties determined from the standard errors of the solution (Table **T2,** p. 26). Also shown are curves showing the stability boundary between methane hydrate and free methane gas for pore water with seawater salinity (3.5%) and the measured salinity at the bottom-simulating reflection (BSR) at this site (3.2%) at hydrostatic pressure. Bounds for each pore water composition show the effect of an uncertainty of ±5 m in water depth. The depth of the BSR is shown with an uncertainty of ±2 m based on the results from the vertical seismic profile at this site (**Tréhu et al.,** this volume).
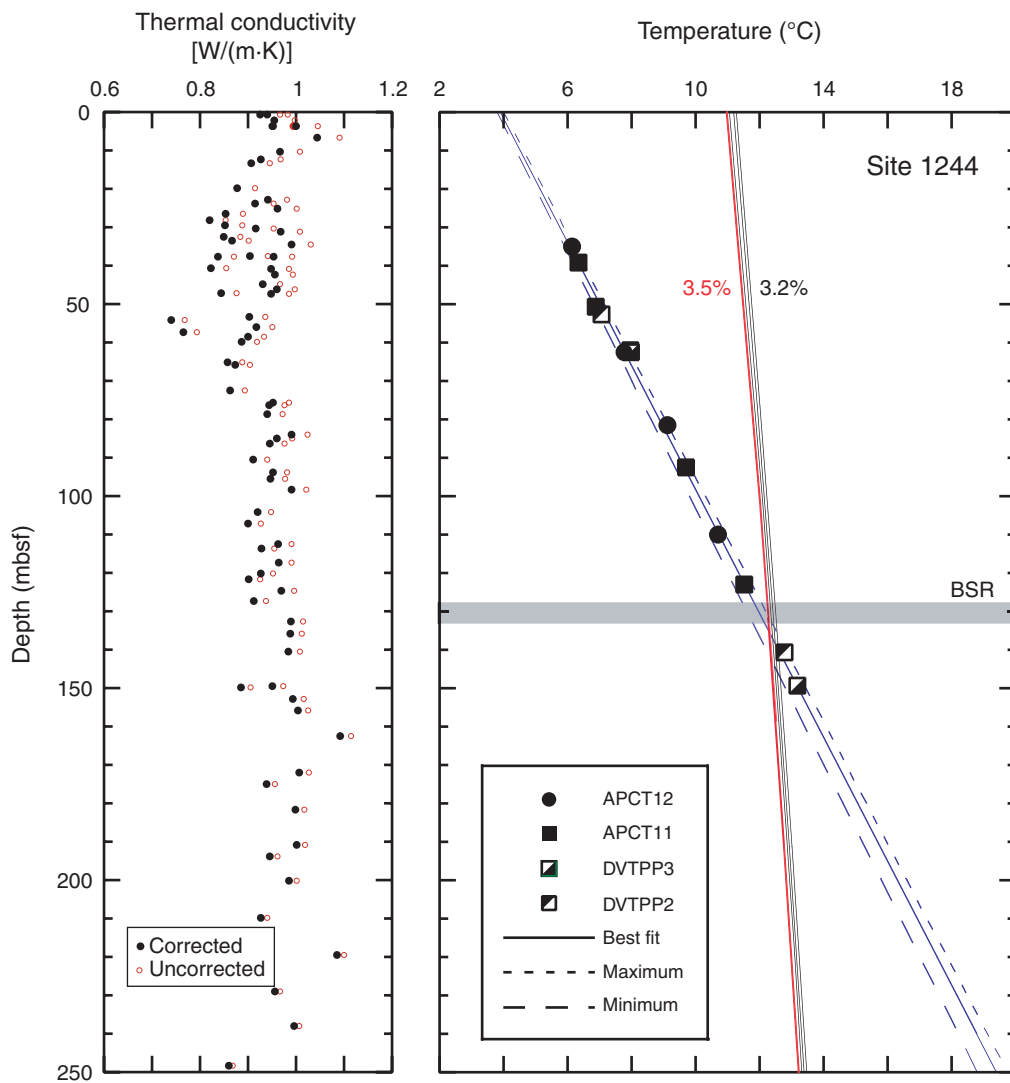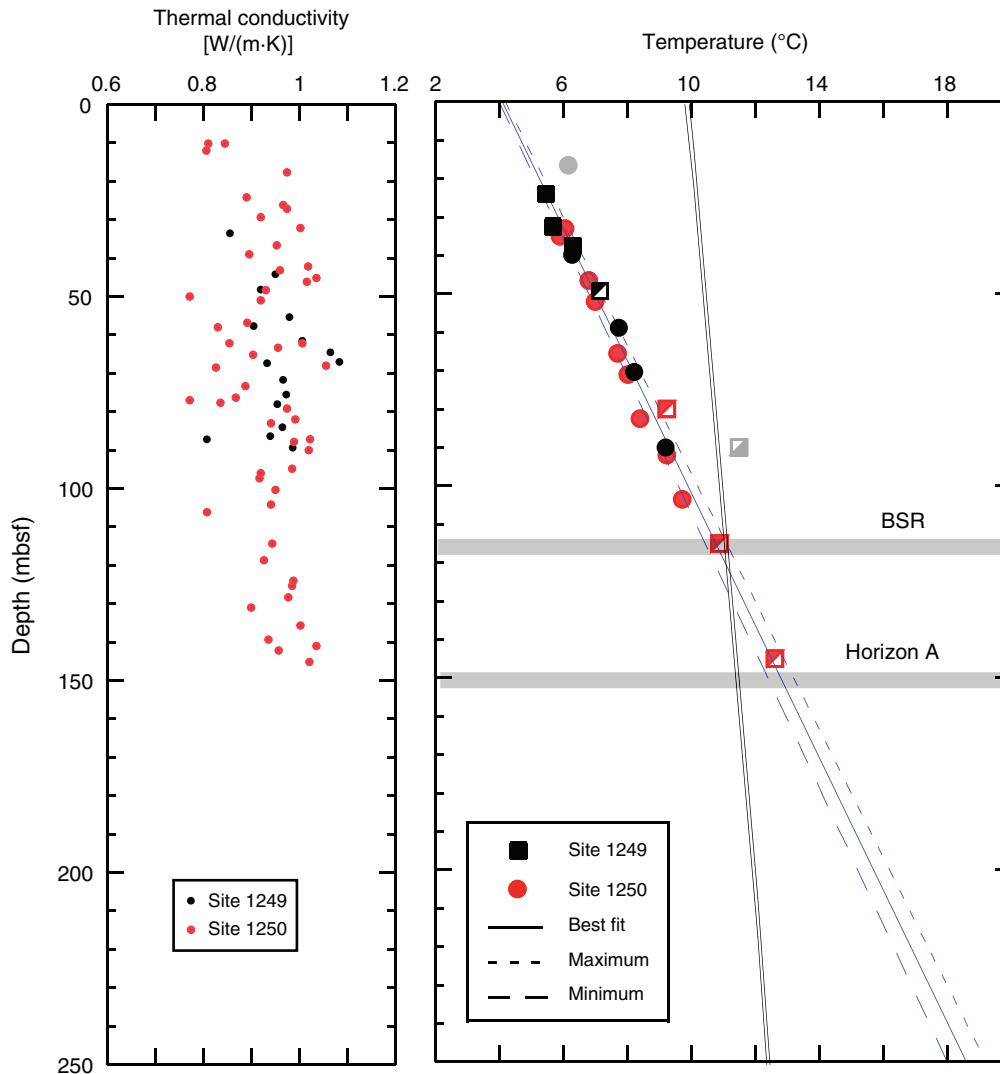
**Figure F6.** Thermal conductivity measured by Advance Piston Corer Temperature (APCT) tool on recovered cores and $T_o$ plotted vs. depth at Site 1245. Each small symbol represents the average of three needle probe measurements corrected to in situ conditions. All in situ temperature estimates have been corrected using the empirically determined calibration constants given in Table T1, p. 25. Overlain on the data is the best-fit linear thermal gradient with uncertainties determined from the standard errors of the solution (Table T2, p. 26). Also shown is the stability boundary between methane hydrate and free methane gas for pore water for the measured salinity at the bottom-simulating reflection (BSR) at this site (3.5%) and at hydrostatic pressure, assuming an uncertainty of ± 5 m in water depth. The depth to the BSR is shown based on sonic log results reported by Guerin et al. (this volume).
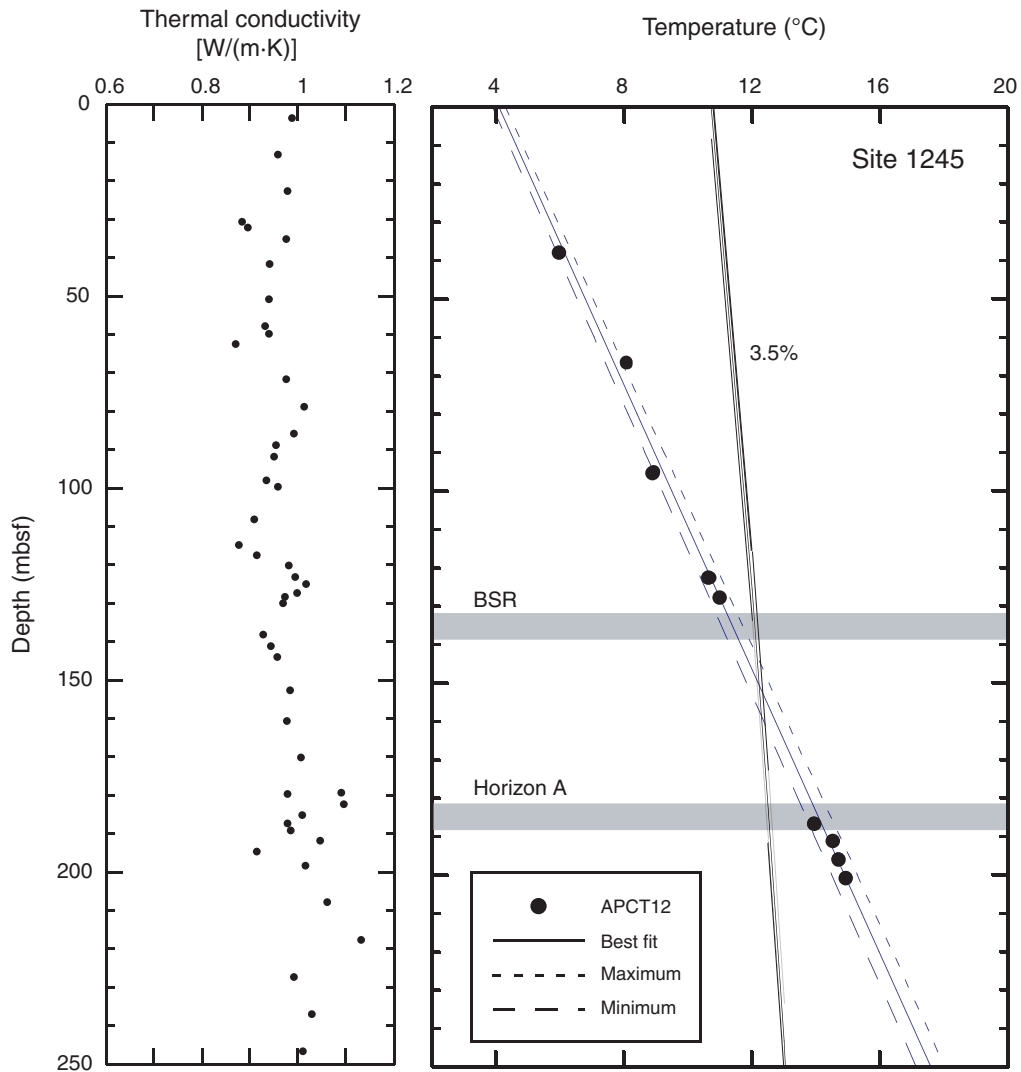
**Figure F7.** Thermal conductivity measured by needle probe on recovered cores and $T_o$ plotted vs. depth at Sites 1247 and 1248. Each small symbol represents the average of three needle probe measurements corrected to in situ conditions. All in situ temperature estimates have been corrected using the empirically determined calibration constants given in Table T1, p. 25. Symbols for different instrument types are the same as in Figure F5, p. 19. Gray symbols represent measurements that were not used because they were considered to be unreliable, either because it was evident that the probe had not penetrated the seafloor (for the DVTP2 and DVTPP2, shown as squares) or because no frictional pulse was observed when the tool was extracted (APTC12 at 17 mbsf). Overlain on the data is the best-fit linear thermal gradient from the combined data set with uncertainties determined from the standard errors of the solution (Table T2, p. 26). Also shown is the stability boundary between methane hydrate and free methane gas for pore water for the measured salinity at the bottom-simulating reflection (BSR) at this site (3.5%) and at hydrostatic pressure assuming an uncertainty of ± 5 m in water depth. The depth to the BSR and to Horizon A at Site 1247 is shown based on the vertical seismic profile reported by Tréhu et al. (this volume). The water depth and BSR depth at Site 1248 are the same as at Site 1247, assuming the velocities are the same. Horizon A at Site 1248 is coincident with the BSR.

**Figure F8.** Thermal conductivity measured by needle probe on recovered cores and $T_o$ plotted vs. depth at Sites 1249 and 1250. Each small symbol represents the average of three needle probe measurements corrected to in situ conditions. All in situ temperature estimates have been corrected using the empirically determined calibration constants given in Table T1, p. 25. Symbols for different instrument types are the same as in Figure F5, p. 19. Gray symbols represent measurements that were not used because they were considered to be unreliable. Overlain on the data is the best-fit linear thermal gradient from the combined data set with uncertainties determined from the standard errors of the solution (Table T2, p. 26). Also shown is the stability boundary between methane hydrate and free methane gas for pore water for the measured salinity at the BSR at this site (3.5%) and at hydrostatic pressure assuming an uncertainty of ± 5 m in water depth. The depth to the BSR and to Horizon A at Site 1250 is shown based on the vertical seismic profile reported by Tréhu et al. (this volume). Site 1249 was only extended to 90 mbsf.

**Figure F9.** Thermal conductivity measured by needle probe on recovered cores and $T_o$ plotted vs. depth at Sites 1251 and 1252. Each small symbol represents the average of three needle probe measurements corrected to in situ conditions. All in situ temperature estimates have been corrected using the empirically determined calibration constants given in Table **T1,** p. 25. Symbols for different instrument types are the same as in Figure **F5,** p. 19. Gray symbols represent measurements that were not used because they were considered to be unreliable. Overlain on the data is the best-fit linear thermal gradient from the combined data set with uncertainties determined from the standard errors of the solution (Table **T2,** p. 26). Gradients are shown using the combined data set for both sites for data from above and below 100 mbsf. Results for other combinations of data are shown in Table **T2,** p. 26. The data are consistent with a constant thermal gradient in a medium with two layers of different thermal conductivity. Similar results would be obtained with other representations of the change in thermal conductivity with depth. The difference between the stability boundary at the two sites is due primarily to the difference in water depth rather than to the difference in pore water salinity. The depth to the bottom-simulating reflection (BSR) at Site 1251 is based on the sonic log (**Guerin et al.,** this volume) and on a strong infrared thermal anomaly observed in the cores (Tréhu et al., 2004a). No BSR is present at Site 1252 (see Fig. **F1B,** p. 14), and the depth shown is projected from observations offset by ~75 m.
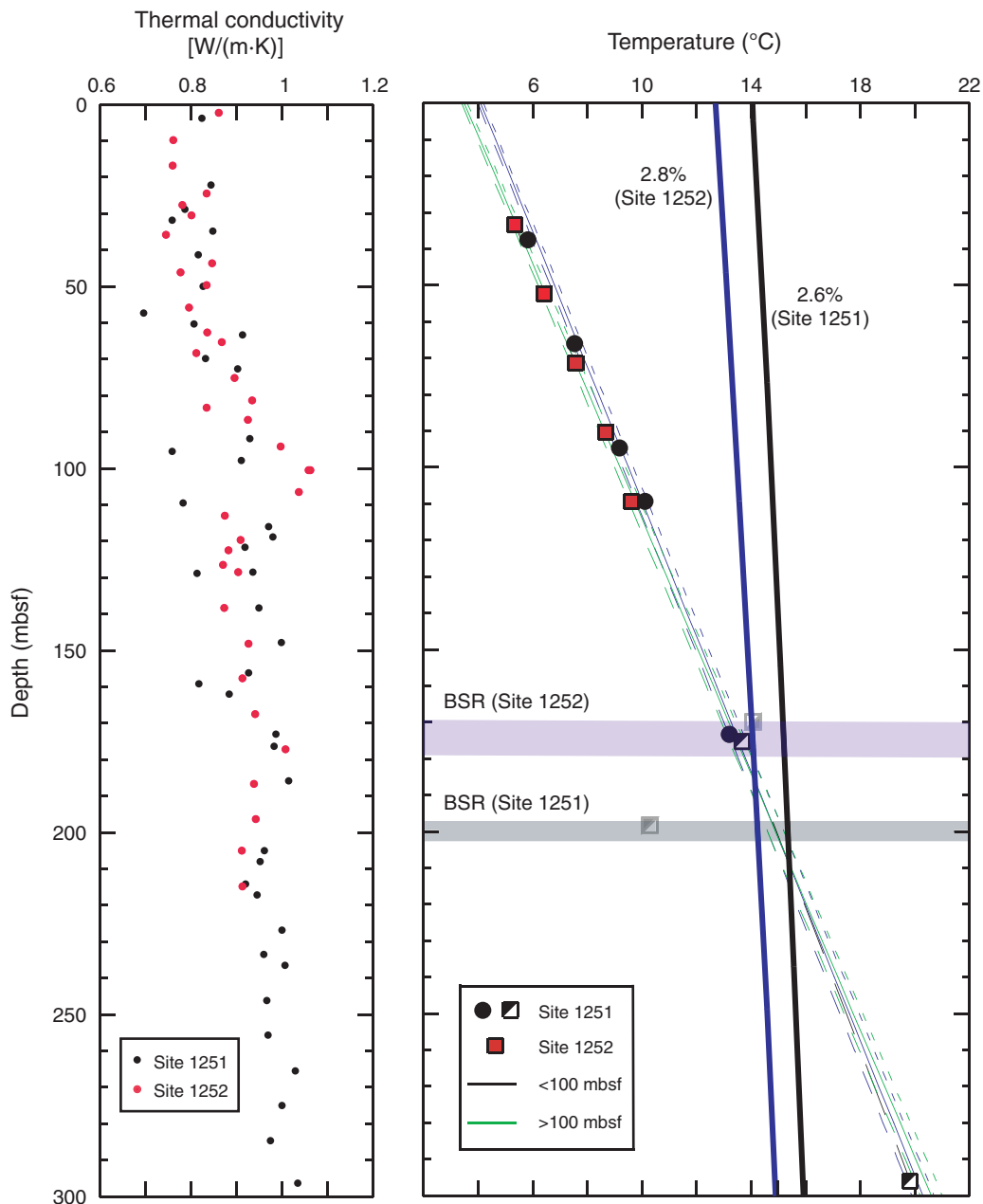
**Figure F10. A.** Heat flow observed at Leg 204 drilling sites compared to heat flow calculated based on the age of the subducting oceanic crust and the thickness of the overlying sediments (thick gray line from Oleskevich et al., 1999). The abrupt decrease in heat flow ~50 km east of the deformation front results from the insulating effect of the low thermal–conductivity Siletz terrain. Heat flow inferred from bottom-simulating reflection (BSR) observations on mid-slope, where the BSR shallows and merges with the seafloor in ~500 m of water (Tréhu et al., 1995), is shown as a dotted line. **B.** Seafloor intercept of the best-fit thermal gradient at each site compared to typical ocean temperature as defined by GLOBEC CTD data from a nearby site as measured 4–5 times/yr in 1999 and 2002.
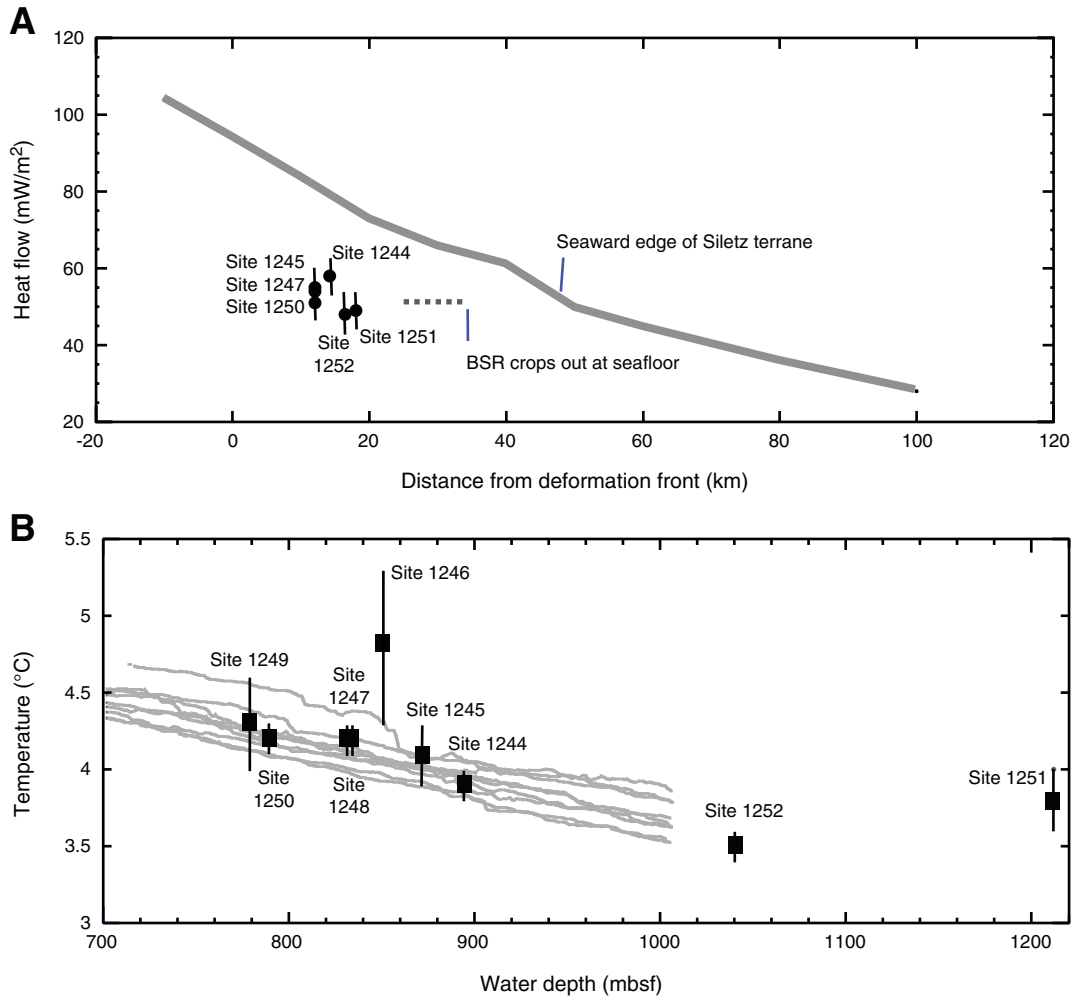
**Table T1.** Calibration factors for instruments used during Leg 204.

| Tool | Calibration correction | Total deployments | Deployments at Site 1244 |
|---|---|---|---|
| APCT11 | –0.51 | 19 | 5 |
| APCT12 (before) | 0 | 34 | 4 |
| APCT12 (after) | –2.5 | 3 | 0 |
| DVTPP2 | 0 | 16 | 2 |
| DVTPP3 | –0.65 | 5 | 2 |
| DVTP2 | 0 | 6 | 0 |

Note: APCT = Advanced Piston Corer Temperature tool, DVTPP = Davis-Villinger Temperature-Pressure Probe, DVTP = Davis-Villinger Temperature Probe.

**Table T2.** Summary of thermal gradients and heat flow observed at southern Hydrate Ridge sites.

| Site | Water depth (m) | Number of $T_o$ estimates (total number of attempts) | $R^2$ | Thermal gradient (°C/km) | Seafloor intercept (°C) | Apparent standard error (°C) | Average thermal conductivity (W/[m·K]) | Heat flow (mW/m²) |
|---|---|---|---|---|---|---|---|---|
| 1244 | 895 | 13 (13) | 1 | 62 ± 1 | 3.9 ± 0.1 | 0.12 | 0.93 ± 0.07 | 58 ± 5 |
| 1245 | 871 | 9 (12) | 1 | 54 ± 1 | 4.1 ± 0.2 | 0.22 | 0.98 ± 0.05 | 54 ± 4 |
| 1246 | 851 | 5 (5) | 0.95 | 55 ± 7 | 4.8 ± 0.5 | 0.46 | 0.93 ± 0.07 | 51 ± 10 |
| 1247 | 830 | 5 (7) | 1 | 53 ± 1 | 4.2 ± 0.1 | 0.08 | 0.96 ± 0.07 | 51 ± 5 |
| 1248 | 830 | 4 (6) | 1 | 54 ± 1 | 4.2 ± 0.1 | 0.04 | 0.98 ± 0.07 | 53 ± 5 |
| 1249 | 780 | 8 (2) | 0.98 | 59 ± 3 | 4.3 ± 0.3 | 0.18 | 0.93 ± 0.07 | 55 ± 7 |
| 1249 | 780 | 5 (>40 mbsf) | 0.98 | 56 ± 5 | 4.0 ± 0.2 | 0.18 | 0.93 ± 0.07 | 52 ± 9 |
| 1250 | 790 | 12 (13) | 0.98 | 59 ± 2 | 4.0 ± 0.2 | 0.27 | 0.94 ± 0.07 | 55 ± 6 |
| 1250 | 790 | 9 (APCT only) | 0.99 | 53 ± 2 | 4.2 ± 0.1 | 0.12 | 0.94 ± 0.07 | 50 ± 6 |
| 1249/1250 | | 21 (23) | 0.97 | 58 ± 2 | 4.1 ± 0.1 | 0.22 | 0.94 ± 0.06 | 55 ± 5 |
| 1251 | 1212 | 7 (9) | 1 | 54 ± 1 | 4.0 ± 0.1 | 0.2 | 0.83/0.95 | 52 ± 8 |
| 1252 | 1040 | 5 (6) | 1 | 57 ± 1 | 3.5 ± 0.1 | 0.07 | 0.84/0.93 | 53 ± 6 |
| 1251/1252 | All | 12 | 1 | 54 ± 1 | 4.1 ± 0.1 | 0.17 | 0.90 ± 0.14 | 49 ± 11 |
| 1251/1252 | <100 mbsf | 7 | 0.99 | 58 ± 2 | 3.8 ± 0.2 | 0.14 | 0.83 ± 0.07 | 48 ± 6 |
| 1251/1252 | >100 mbsf | 5 | 1 | 52 ± 1 | 4.4 ± 0.2 | 0.16 | 0.94 ± 0.06 | 49 ± 4 |

Note: APCT = advanced piston corer temperature tool.